Journal of
Materials Chemistry A

PAPER

View Article Online
View Journal

Cite this: DOI: 10.1039/d6ta01695b

Vacancy-mediated dual-step phosphorization-sulfurization of $MnMoO_4$ for efficient acidic hydrogen evolution

Jyoti Ganapati Badiger,[a] Chae-Eun Lim,[b] Fawad Tariq,[c] Maheswari Arunachalam,[d] Suzan Abdelfattah Sayed,[e] Alaa M. Ibrahim,[a] Sang-Wan Ryu,[c] Byung-Hyun Kim *[b] and Soon Hyung Kang *[d]

Received 26th February 2026
Accepted 19th March 2026

DOI: 10.1039/d6ta01695b

rsc.li/materials-a

Developing efficient and acid-stable electrocatalysts from earth-abundant materials remains a central challenge for sustainable hydrogen production. Here, we propose a vacancy-mediated dual-step anion engineering strategy, in which sequential phosphorization and sulfurization cooperatively modulate the electronic structure of $MnMoO_4$ for acidic hydrogen evolution. Phosphorus incorporation thermodynamically promotes oxygen-vacancy formation, while subsequent sulfur occupation stabilizes defect sites and optimizes the surface coordination environment, yielding a heteroatom-enriched P,S–$MnMoO_4$ catalyst. As a result, P,S–$MnMoO_4$ delivers a low overpotential of 198 mV at 10 mA cm^{-2} in 0.5 M H_2SO_4 and maintains stable operation over 50 h. Spectroscopic and electrochemical analyses reveal enhanced charge-transfer kinetics and an enlarged electrochemically active surface area induced by cooperative anion incorporation. Density functional theory calculations further demonstrate that P–S co-incorporation strengthens orbital hybridization between active sites and adsorbed H*, achieving a near-optimal hydrogen adsorption free energy and lowering the thermodynamic barrier for the Volmer step. This work establishes a generalizable anion-relay design paradigm for activating metal oxides toward efficient acidic HER.

1. Introduction

Developing clean and sustainable hydrogen production technologies is crucial for addressing global energy and environmental challenges.[1] Among various energy carriers, molecular hydrogen (H_2) has attracted considerable attention owing to its high gravimetric energy density and carbon-free nature.[2] However, the current industrial production of hydrogen is still dominated by steam reforming of fossil fuels, an energy-intensive process accompanied by substantial CO_2 emissions.[3] In this regard, electrochemical water splitting, particularly the hydrogen evolution reaction (HER), offers a promising and environmentally benign pathway for hydrogen generation.[4] Nevertheless, the practical deployment of HER remains limited by sluggish reaction kinetics, necessitating the development of highly efficient electrocatalysts.[5] Platinum-based materials are widely recognized as benchmark HER catalysts because of their near-optimal hydrogen adsorption free energy and low overpotentials. However, their scarcity and prohibitive cost severely restrict large-scale applications.[6] Consequently, extensive efforts have been devoted to developing earth-abundant alternatives based on transition metals such as Mo, Ni, Co, and Mn. In this context, non-noble metal compounds including oxides, sulfides, phosphides, and nitrides have emerged as promising candidates. Among them, transition-metal molybdates (*e.g.*, $NiMoO_4$,[7] $CoMoO_4$,[8] and $MnMoO_4$ (ref. 9)) have garnered significant interest due to their multiple redox-active centers, structural robustness, and compositional tunability.

Particularly, $MnMoO_4$ stands out as an attractive HER catalyst owing to the intrinsic activity of Mn species and the synergistic electronic interactions between Mn and Mo centers, combined with its natural abundance and low toxicity.[10] Despite these advantages, pristine $MnMoO_4$ typically suffers from low electrical conductivity and limited exposure of catalytically active sites, leading to unsatisfactory HER performance.[11] To address these intrinsic limitations, various strategies such as surface modification,[12] heterostructure construction,[13] defect engineering,[9] and polymer composite formation[14] have been

---

[a] *Department of Interdisciplinary Program for Photonic Engineering, Chonnam National University, Gwangju 61186, Republic of Korea*

[b] *Department of Applied Chemistry, Center for Bionano Intelligence Education and Research, Hanyang University, ERICA, Ansan, 15588, Republic of Korea. E-mail: bkkim00@hanyang.ac.kr*

[c] *Department of Physics, Chonnam National University, Gwangju 61186, Republic of Korea*

[d] *Department of Chemistry Education and Optoelectronic Convergence Research Center, Chonnam National University, Gwangju 61186, Republic of Korea. E-mail: skang@jnu.ac.kr*

[e] *Department of Chemical Engineering, Chonnam National University, Gwangju 61186, Republic of Korea*

explored. For instance, partial amorphization *via* hydrogenation has been shown to enhance HER activity by increasing defect density,[11] while conductive polymer wrapping has improved charge transport and reduced overpotential to 155 mV at 10 mA cm^{-2}.[15] These studies collectively demonstrate that electronic structure modulation and defect control are key to activating $MnMoO_4$ for HER.

Building on this understanding, a more fundamental challenge lies in how to cooperatively engineer defect states and anion coordination environments to optimize hydrogen adsorption under acidic conditions. Herein, we introduce a dual-step phosphorization–sulfurization strategy as a vacancy-mediated anion engineering approach to activate $MnMoO_4$ for efficient acidic HER. Phosphorization thermodynamically promotes oxygen-vacancy formation by disrupting Mn–O and Mo–O bonds, while subsequent sulfurization stabilizes these vacancy sites and further modulates the local electronic structure. This cooperative anion incorporation generates a heteroatom-enriched, conductive surface with accelerated charge-transfer kinetics and increased density of accessible active sites. As a result, the optimized P,S–$MnMoO_4$ catalyst delivers an overpotential of 198 mV at 10 mA cm^{-2} in 0.5 M H_2SO_4, a low Tafel slope of 75 mV dec^{-1}, and stable operation over 50 h. This work thus establishes a vacancy-mediated anion-relay design strategy for activating metal oxides toward high-performance, acid-stable HER electrocatalysis.

2. Experimental section

2.1. Materials

All chemicals were used without further purification. Ammonium molybdate tetrahydrate $(NH_4)_6Mo_7O_{24}$ $4H_2O$, 99.98%, sigma-Aldrich), manganese(II) nitrate tetrahydrate (Mn $(NO)_3$ $2(H_2O)_4$, ≥97% sigma-Aldrich), and sodium hypophosphate monohydrate (NaH_2PO_2 H_2O) were purchased from Sigma-Aldrich. Carbon cloth (0.33 mm thickness, basic weight 120 g m^{-2}) was used as the conductive substrate.

2.2. Synthesis of $MnMoO_4$

$MnMoO_4$ was synthesized using a hydrothermal method. Prior to synthesis, carbon cloth (CC) was ultrasonically cleaned and then treated in a mixed solution of sulfuric acid and nitric acid (volume ratio 1 : 1) at 80 °C for 1 h to improve surface hydrophilicity. Specifically, 0.05 M of $(NH_4)_6Mo_7O_{24}$ $4H_2O$ and 0.05 M of (Mn $(NO)_3$ $2(H_2O)_4$) were dissolved separately in 20 mL of deionized (DI) water and stirred for 15 min. each. The manganese nitrate solution was then added dropwise into the ammonium molybdate solution under continuous stirring, followed by additional stirring for 15 min. To ensure homogeneous mixing. The resulting solution was transferred into a 50 mL Teflon-lined stainless-steel autoclave, and a pretreated carbon cloth substrate was immersed vertically in the autoclave at an inclined angle. The autoclave was then sealed and placed in an oven at 180 °C for 12 h. After naturally cooling to room temperature, the samples were thoroughly washed with DI water and dried in ambient conditions. The obtained samples were denoted as $MnMoO_4$.

2.3. Phosphorization of $MnMoO_4$

Phosphorization was carried out in a tube furnace under an argon atmosphere to introduce phosphorus into the $MnMoO_4$ lattice. The NaH_2PO_2 H_2O was employed as the phosphorus source and placed upstream of the furnace, while the $MnMoO_4$ samples were positioned downstream, as illustrated in Fig. 1. Furnace temperature was ramped to 400 °C and maintained for 1 h. After cooling to room temperature under Ar flow, the phosphorized samples were collected and designated as P–$MnMoO_4$.

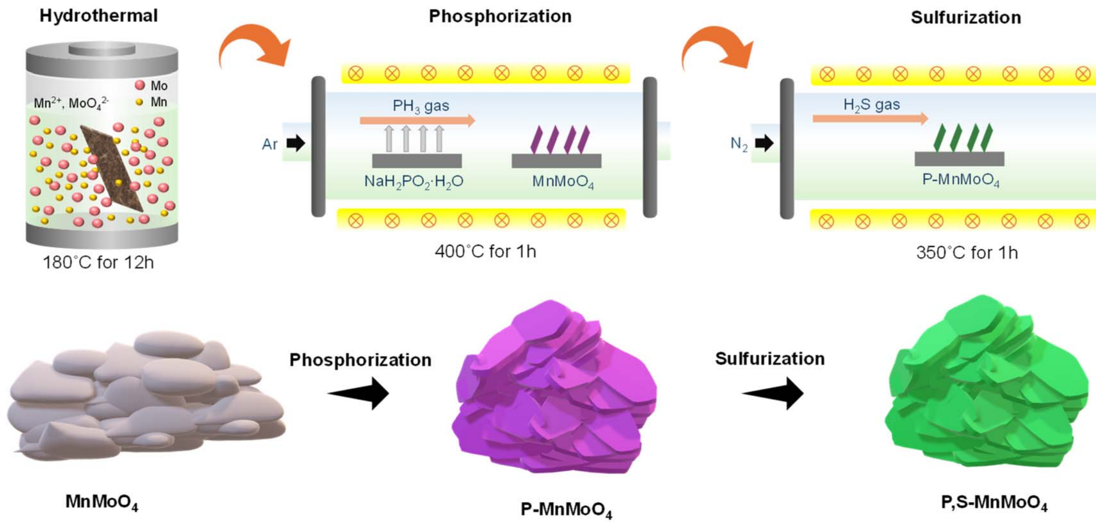

Fig. 1 Schematic illustration of the vacancy-mediated anion relay mechanism during the sequential phosphorization and sulfurization of $MnMoO_4$.

2.4. Sulfurization of $MnMoO_4$

Sulfurization was performed using the phosphorized $MnMoO_4$ as the precursor. P–$MnMoO_4$ samples were placed in a tube furnace and treated at 350 °C under a flowing H_2S atmosphere to introduce sulfur *via* a solid–gas reaction. After cooling, the obtained samples were labeled as P,S–$MnMoO_4$. For comparison, sulfurized $MnMoO_4$ samples without the intermediate phosphorization step were also prepared under identical sulfurization conditions and denoted as S–$MnMoO_4$.

2.5. Material characterizations

The surface morphology and elemental distribution of $MnMoO_4$, P–$MnMoO_4$ and P,S–$MnMoO_4$ was systematically analyzed using field-emission scanning electron microscopy (FE-SEM with EDS: SU5000, HITACHI Inc.), operated at an accelerating voltage of 10 kV. The crystalline and phase properties were rigorously evaluated with high-resolution X-ray diffraction (HR-XRD) utilizing a PANalytical X'Pert PRO MRD instrument, operating at 40 kV and 30 mA. Raman spectroscopy (NRS-5100, JASCO) with a 532 nm laser was used to probe lattice vibrations and structure changes induced by phosphorus and sulfur incorporation. Electron spin resonance (ESR) measurements were carried out using an EMXplus-9.5/12/P/L spectrometer with a field modulation frequency of 100 kHz to analyze defect states. X-ray photoelectron spectroscopy (XPS, Mg Kα source) was conducted to investigate the elemental composition and chemical states between the $MnMoO_4$, P–$MnMoO_4$ and P,S–$MnMoO_4$ samples.

2.6. Electrochemical measurements

Electrochemical hydrogen evolution reaction (HER) measurements were executed using a standard three-electrode setup with 1×1 cm^2 electrodes. The as-prepared electrocatalyst served as the working electrode, with a graphite rod as the counter electrode and a saturated Ag/AgCl electrode as the reference. All measurements were conducted in N_2-saturated 0.5 M H_2SO_4 electrolyte. Linear sweep voltammetry (LSV) was recorded at a scan rate of 5 mV s^{-1}. The measured potentials were converted to the reversible hydrogen electrode (RHE) scale using the following eqn (1):

$$E_{\mathrm{RHE}} = E_{\mathrm{Ag/AgCl(sat.)}} + E^{\circ}_{\mathrm{Ag/AgCl(sat.)}} + 0.0591 \times \mathrm{pH} \tag{1}$$

where the standard potential $E^{\circ}_{\mathrm{Ag/AgCl}}$ was taken as 0.210 V at room temperature, and the electrolyte pH was 0.34. All polarization curves were corrected for ohmic losses (iR correction), and Tafel slopes were derived from linear fitting of the polarization data. Electrochemical impedance spectroscopy (EIS) was performed at open-circuit potential over a frequency range of 0.1 Hz to 10 kHz with an AC amplitude of ±10 mV using an AUTOLAB PGSTAT128N potentiostat. The electrochemically active surface area (ECSA) was estimated from the double-layer capacitance (C_{dl}) obtained by cyclic voltammetry (CV) measurements conducted at scan rates of 20–100 mV s^{-1} within a non-faradaic potential window of 0.0–0.3 V *vs.* Ag/AgCl. Long-term stability was evaluated by chronopotentiometry at a constant current densities of 10, 50 , and 100 mA cm^{-2}.

2.7. Computational method

All structural relaxation and electronic structure calculations were carried out within the framework of spin-polarized density functional theory (DFT) using the Vienna *Ab initio* Simulation Package (VASP).[16–18] The generalized gradient approximation (GGA)[19] with the Perdew–Burke–Ernzerhof (PBE)[20] exchange–correlation functional was employed to describe electron–electron interactions. Long-range dispersion forces were included in all calculations using Grimme's D3 dispersion correction with zero-damping function.[21] The projector-augmented wave (PAW) method[20] was adopted to describe the electron-ion interactions, explicitly treating the Mn (3p, 3d, 4s), Mo (4p, 4d, 5s), O (2s, 2p), P (3s, 3p), S (3s, 3p), and H (1s) orbitals as valence states. A plane-wave kinetic-energy cutoff of 500 eV was used for all systems. The electronic energy convergence and force convergence criteria for geometry optimization were set at 10^{-6} eV and 0.02 eV Å^{-1}, respectively. Brillouin-zone integrations were performed using Monkhorst–Pack *k*-point meshes of $6 \times 6 \times 6$ for bulk models and $3 \times 3 \times 1$ for slab models.[22] Among the three reported polymorphs of $MnMoO_4$, the monoclinic β-$MnMoO_4$ phase was chosen as the reference of bulk structure.[23,24] This choice is supported by comparison between the XRD pattern measured in this work and previously reported XRD data for $MnMoO_4$ phases.[25] To account for the localized nature of Mn-3d and Mo-4d electrons, the GGA + *U* approach was implemented within the Dudarev formalism that has been simplified.[26] Effective Hubbard + *U* parameters were adopted (U = 4.0, 6.3 eV for Mn and Ni, respectively), following previously reported values for Mn- and Mo-based oxide systems.[27–30] Based on the optimized β-$MnMoO_4$ bulk structure, a series of low-index surfaces was constructed to investigate the relative stability of different facets. Stoichiometric slab models were generated by cleaving the relaxed bulk along the (010), (001), (101), and (111) planes. To determine the surface structures, the surface free energies of the (010), (001), (101), and (111) planes were calculated. A vacuum spacing of 15 Å was introduced above the slab along the surface to reduce spurious interactions between periodically repeated images. The surface free energy γ was evaluated according to the eqn (2):

$$\gamma = \frac{(E_{\mathrm{slab}} - N \cdot E_{\mathrm{bulk}})}{2A} \tag{2}$$

where E_{slab} is the total energy of the slab, E_{bulk} is the energy per formula unit of bulk β-$MnMoO_4$, N is the number of formula units contained in the slab, and A is the surface area of one side of the slab. Among the investigated facets, the (001) surface exhibited the lowest surface free energy and was thus chosen as the basis for all $MnMoO_4$-based surface models in the subsequent hydrogen-adsorption and electronic-structure analysis. To gain mechanistic insight into the origin of the superior HER activity of P,S–$MnMoO_4$, comprehensive DFT calculations were conducted on a series of $MnMoO_4$-based surfaces.

In acidic media, the hydrogen evolution reaction (HER, $2H^+ + 2e^- \rightarrow H_2$) proceeds through the formation and subsequent removal of a chemisorbed hydrogen intermediate (H*), as described by the classical Volmer–Heyrovsky–Tafel mechanism:[31]

$$H^+ + e^- + * \rightarrow H^* \text{ (Volmer)} \tag{3}$$

$$H^+ + e^- + H^* \rightarrow H_2 + * \text{ (Heyrovsky)} \tag{4}$$

$$2H^* \rightarrow H_2 + 2^* \text{ (Tafel)} \tag{5}$$

where * and H* denote an empty active site and a chemisorbed hydrogen atom on the catalyst surface, respectively. Here, eqn (3) corresponds to the Volmer step, while eqn (4) and (5) represent the Heyrovsky and Tafel steps, respectively. In this framework, hydrogen gas is generated through a sequence of proton–electron transfer and subsequent desorption steps, and the adsorption and desorption of H* represent competitive processes that are strongly governed by the intrinsic electronic structure of the catalyst. According to the Sabatier principle, an ideal HER catalyst binds H* neither too strongly nor too weakly, the interaction must be sufficiently strong to facilitate proton–electron transfer but weak enough to allow facile H_2 release.[32] As direct experimental quantification of the H-surface bond strength is challenging, the hydrogen adsorption Gibbs free energy (ΔG_{H^*}) is widely adopted as a thermodynamic descriptor, and values close to zero are generally correlated with optimal HER performance.[32,33] In this study, ΔG_{H^*} was evaluated following the standard free-energy scheme (eqn (6) and (7)) for HER electrocatalysts.[33]

$$\Delta G = E_{\text{ads}} + \Delta E_{\text{ZPE}} - T\Delta S \tag{6}$$

$$E_{\text{ads}} = E_{H^*} - E_{\text{surface}} - \frac{1}{2}E_{H_2} \tag{7}$$

where ΔZPE is defined as the zero-point energy difference between the clean surface and the adsorbed species, T denotes the absolute temperature, and ΔS corresponds to the change in entropy. The thermodynamic quantities for the adsorbed molecules were evaluated from DFT calculations at room temperature.

3. Results and discussion

3.1. Vacancy-mediated anion relay mechanism during sequential phosphorization and sulfurization of $MnMoO_4$

The phosphorization treatment is generally considered to proceed through a gas–solid reaction pathway, as reported in the literature.[34] Thermal decomposition of $NaH_2PO_2 \cdot H_2O$ can generate phosphine (PH_3) and water vapor under an inert atmosphere, where PH_3 may serve as a reducing phosphorus source. Under such conditions, interactions between PH_3 and the $MnMoO_4$ lattice have been suggested to promote partial reduction of the oxide surface and the formation of oxygen-deficient regions. In the presence of water vapor, phosphorus-containing species (*e.g.*, H_3PO_4 or phosphate-derived anions) may form and participate in surface ion-exchange or adsorption processes. It has been proposed that phosphate species could be incorporated into the near-surface region of oxygen-deficient $MnMoO_4$ through gradual diffusion or interfacial exchange with surface hydroxyl groups. While the detailed incorporation mechanism is not directly probed in this work, this reaction scheme provides a plausible description consistent with previous reports.[34]

The overall reactions can be represented as follows (eqn (8)–(11)):

$$NaH_2PO_2 \cdot H_2O \rightarrow PH_3 \uparrow + Na_2HPO_4 + H_2O \uparrow \tag{8}$$

$$MnMoO_4 + xPH_3 \rightleftharpoons MnMoO_{4-4x} + xH_3PO_4 \tag{9}$$

$$H_2O + PO_4^{3-} \rightleftharpoons HPO_4^{2-} + OH^- \tag{10}$$

$$HPO_4^{2-} + H_2O \rightleftharpoons H_2PO_4^- + OH^- \tag{11}$$

where x represents the number of oxygen atoms removed from the lattice, thereby leading to the increased concentration of oxygen vacancies generated during phosphorization. The subsequent sulfurization step using the phosphorized $MnMoO_{4-4x}$, at 350 °C under an H_2S atmosphere, enables sulfur atoms to preferentially interact with the pre-formed oxygen-vacancy sites. This solid–gas reaction partially substitutes lattice oxygen with sulfur, stabilizing defect sites and further modulating the local coordination environment and electronic structure of $MnMoO_4$, as expressed by the eqn (12):

$$MnMoO_{4-4x} + yH_2S \rightarrow MnMoO_{4-4x-y}S_y + yH_2O \tag{12}$$

Here, x represents pre-existing oxygen vacancies generated during the phosphorization step, while y denotes the number of oxygen atoms replaced by sulfur. This sequential process establishes a vacancy-mediated anion relay mechanism, in which phosphorus incorporation promotes oxygen-vacancy formation and subsequent sulfur occupation stabilizes these defect sites, collectively governing the electronic-structure evolution of $MnMoO_4$. Detailed spectroscopic, electrochemical, and theoretical analyses supporting this mechanism are discussed in the Results and Discussion section.

3.2. Structural and electronic characterization of $MnMoO_4$-based electrocatalysts

Fig. 2 presents FE-SEM images and corresponding elemental mapping of $MnMoO_4$, P–$MnMoO_4$, and P,S–$MnMoO_4$ electrocatalysts. As shown in Fig. 2(a), pristine $MnMoO_4$ exhibits a hierarchical plate-like morphology with interspersed microrod structures. Notably, this morphological framework is well preserved after phosphorization (Fig. 2(e)) and subsequent sulfurization (Fig. 2(j)), indicating that the sequential anion incorporation does not induce structural collapse or morphological degradation. The retention of the original morphology suggests that the dual-step phosphorization–sulfurization process primarily modifies the surface chemistry and electronic structure rather than the bulk architecture.

Elemental mapping further confirms the compositional evolution of the $MnMoO_4$-based electrocatalysts. Uniform distributions of Mn, Mo, and O are observed for pristine $MnMoO_4$ (Fig. 2(b–d)). After phosphorization, the emergence of homogeneously distributed phosphorus signals (Fig. 2(f–i)) indicates successful P incorporation across the $MnMoO_4$

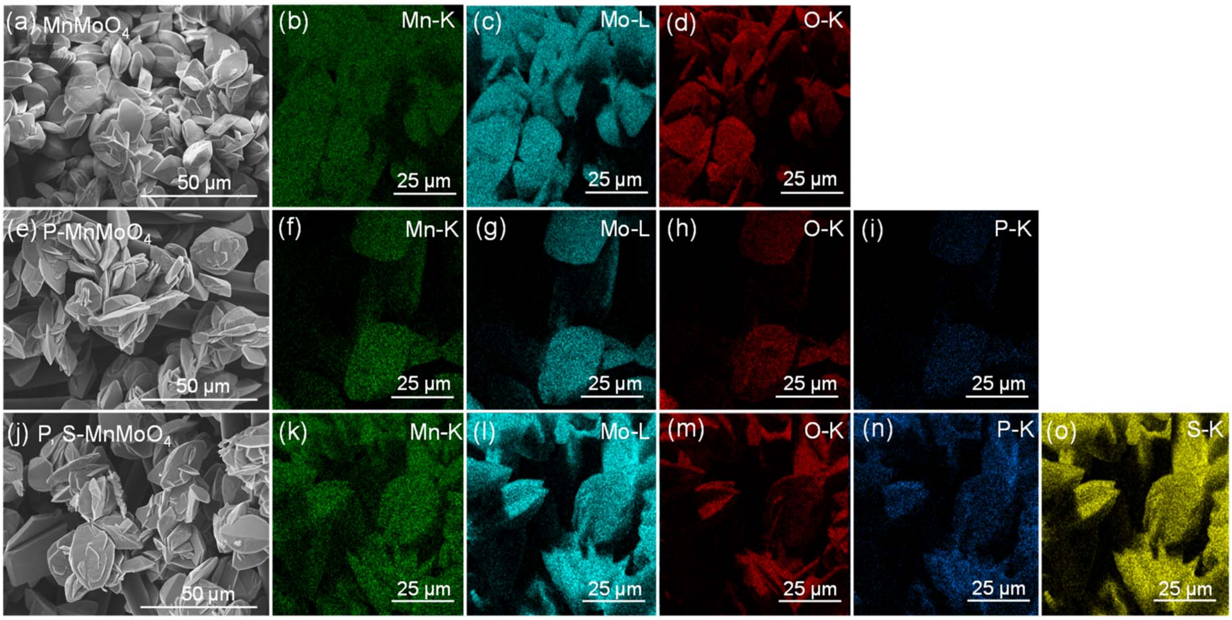

Fig. 2 FE-SEM images and corresponding elemental mapping of (a–d) $MnMoO_4$, (e–i) P–$MnMoO_4$ and (j–o) P,S–$MnMoO_4$ electrocatalysts.

surface. Following sulfurization, additional sulfur signals are clearly detected and uniformly distributed in P,S–$MnMoO_4$ (Fig. 2(k–o)) and demonstrating effective sulfur incorporation without phase segregation. These results, together with the EDX spectra shown in Fig. S1, confirm the homogeneous incorporation of P and S within the $MnMoO_4$ framework, providing a structural basis for the subsequent modulation of defect chemistry and electronic structure. Furthermore, FE-SEM analysis together with the corresponding elemental mapping was performed for S–$MnMoO_4$, as shown in Fig. S2. The images show that the plate-like morphology of $MnMoO_4$ is largely preserved after the sulfurization process, suggesting that the overall structural framework remains intact. In addition, elemental mapping and EDX spectra demonstrate the presence and homogeneous distribution of sulfur throughout the sample, supporting the successful sulfur modification of $MnMoO_4$ without noticeable morphological degradation.

Fig. 3(a) shows the X-ray diffraction (XRD) patterns of the carbon cloth substrate and $MnMoO_4$-based electrocatalysts. The diffraction peaks marked with asterisks (*) originate from the carbon cloth substrate and are consistent with the standard pattern (JCPDS No. 00-020-058). Pristine $MnMoO_4$ exhibits well-defined diffraction peaks at 2θ values of 15.39°, 18.46°, 23.63°, 29.95°, 30.31°, 36.06°, 37.37°, 40.79°, and 51.22°, which can be indexed to the (010), (100), (011), (111), (−111), (021), (200), (−121), and (130) planes of monoclinic $MnMoO_4$ (JCPDS No. 00-015-0791), confirming the formation of a phase-pure $MnMoO_4$ structure.

After phosphorization, the diffraction peaks of P–$MnMoO_4$ exhibit a slight shift toward lower 2θ angles relative to pristine $MnMoO_4$, indicating lattice expansion induced by phosphorus incorporation. This structural distortion suggests the introduction of heteroatoms and defect states into the $MnMoO_4$ lattice rather than a complete phase transformation. The enlarged XRD patterns (Fig. 3(b) and S3) reveal weak but discernible diffraction peaks at 26.11°, 32.96°, and 33.63°. These features may be associated with minor secondary phases such as MnP or slight structural perturbations following P and S incorporation. In addition, as shown in Fig. S3, subtle peak shifts and intensity variations of $MnMoO_4$ reflections are observed after modification, which may indicate lattice distortion or structural modification. However, no major phase transformation is detected, and the overall $MnMoO_4$ framework remains preserved. The emergence of these peaks implies partial cleavage of Mn–O bonds and the formation of Mn–P bonds during phosphorization, consistent with the generation of oxygen vacancies.

Following sulfurization, the P,S–$MnMoO_4$ electrocatalyst exhibits additional peak shifts toward higher 2θ angles compared to P–$MnMoO_4$, suggesting lattice distortion or partial contraction associated with sulfur incorporation. Notably, the MnP-related diffraction features remain detectable after sulfurization, indicating that the Mn–P bonding framework formed during phosphorization is preserved during the subsequent sulfurization step. These observations support a sequential anion incorporation process in which phosphorus-induced lattice expansion and vacancy formation are followed by sulfur-mediated structural reorganization without collapse of the $MnMoO_4$ crystalline framework.

Fig. 3(c) shows the Raman spectra of $MnMoO_4$, P–$MnMoO_4$, and P,S–$MnMoO_4$ electrocatalysts, providing insight into lattice vibrations and local bonding environments. Pristine $MnMoO_4$ exhibits characteristic phonon modes at approximately 820, 849, and 929 cm^{-1}, which are assigned to asymmetric Mo–O stretching, Mo–O–Mo bridging vibrations, and terminal Mo=O stretching modes within the MoO_4 tetrahedra, respectively. Upon phosphorization, these Raman bands exhibit noticeable shifts relative to pristine $MnMoO_4$, indicating perturbation of

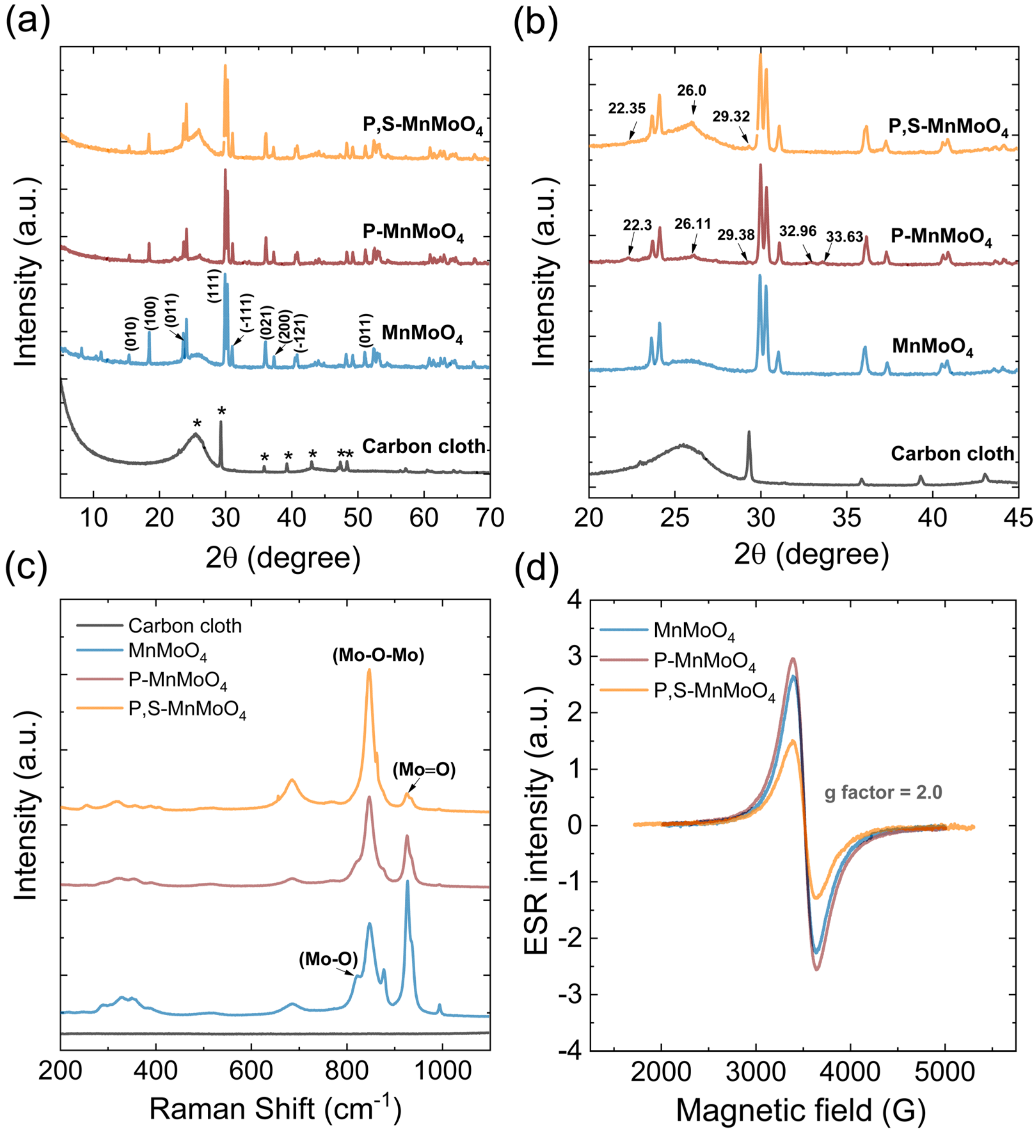

Fig. 3 (a and b) XRD patterns and magnified XRD profiles, (c) Raman spectra, and (d) ESR spectra of $MnMoO_4$, P–$MnMoO_4$ and P,S–$MnMoO_4$ electrocatalysts, revealing lattice distortion and defect evolution induced by sequential phosphorization and sulfurization.

the lattice vibrational symmetry induced by phosphorus incorporation. Such spectral changes suggest modification of the local chemical environment and bonding configuration of Mo–O units, consistent with phosphorus-induced lattice distortion and defect formation. Following sulfurization, further shifts of the Raman peaks are observed, reflecting additional structural distortion arising from the cooperative incorporation of phosphorus and sulfur. Notably, the intensity of the Mo═O stretching mode at ~929 cm^{-1} is markedly reduced after phosphorization and continues to diminish upon sulfurization, implying progressive weakening of terminal Mo–O bonds. In parallel, the emergence of a new Raman feature near 700 cm^{-1} is attributed to the formation of P–O bonds. The persistence of this band after sulfurization suggests that the P–O coordination remains structurally stable during the dual-step anion incorporation process.

Fig. 3(d) displays the electron spin resonance (ESR) spectra of $MnMoO_4$-based electrocatalysts, providing insight into defect states and paramagnetic centers. Pristine $MnMoO_4$ exhibits a prominent ESR signal with a g-factor of approximately 2.0, which is commonly associated with Mn^{2+} species and defect-related paramagnetic centers arising from lattice distortions and oxygen vacancies.[35]

Upon phosphorization, the ESR signal intensity of P–$MnMoO_4$ increases noticeably, suggesting an enhanced concentration of paramagnetic centers. This increase can be attributed to phosphorus-induced defect generation, particularly the formation of oxygen vacancies accompanied by partial electronic redistribution around Mn and Mo centers, consistent with the lattice distortion observed in XRD and Raman analyses.

In contrast, sulfurization leads to a significant decrease in ESR signal intensity for P,S–$MnMoO_4$. This reduction implies partial passivation of oxygen-vacancy-related defect sites by sulfur incorporation, which stabilizes the local coordination environment and reduces the density of unpaired spins. Such defect modulation indicates a transition from vacancy generation to vacancy stabilization, highlighting the cooperative role of phosphorus and sulfur in regulating the defect chemistry of $MnMoO_4$. These controlled defect states are expected to favorably influence charge-transfer characteristics and hydrogen adsorption behavior, thereby contributing to the enhanced HER activity observed for P,S–$MnMoO_4$.

To investigate the elemental composition and chemical states of the prepared electrocatalysts, X-ray photoelectron spectroscopy (XPS) analysis was performed on $MnMoO_4$, P–$MnMoO_4$, and P, S–$MnMoO_4$ electrocatalyst. The wide-scan survey spectra (Fig. S4) confirm the presence of Mn, Mo, and O in all samples, while additional P and S signals appear after phosphorization and sulfurization, respectively. The high-resolution Mn 2p XPS spectra of $MnMoO_4$-based electrocatalysts are presented in Fig. 4(a). For pristine $MnMoO_4$, two dominant peaks located at 640.95 eV and 651.97 eV are observed, corresponding to the Mn $2p_{3/2}$ and Mn $2p_{1/2}$ levels of Mn^{2+}, respectively, with an energy separation of approximately 11.0 eV, characteristic of divalent manganese. In addition, weaker components at 643.53 eV (Mn $2p_{3/2}$) and 655.44 eV (Mn $2p_{1/2}$) are detected, which can be attributed to Mn^{4+} species, likely caused by surface oxidation during synthesis or air exposure.[36] After phosphorization, the Mn $2p_{3/2}$ and Mn $2p_{1/2}$ peaks assigned to Mn^{2+} shift positively to 642.46 eV and 654.41 eV, respectively. This pronounced positive shift ($\approx$+1.5 eV) indicates a decrease in local electron density around Mn centers induced by phosphorus incorporation. Simultaneously, the Mn^{4+}-related components become negligible, suggesting a reduction-dominated process associated with oxygen-vacancy formation and cleavage of Mn–O bonds during phosphorization. Moreover, the appearance of distinct satellite features at 647.3 eV and 659.4 eV further confirms the presence of Mn^{2+} with strong multiplet splitting, reflecting significant electronic reconfiguration of Mn centers.[37] Upon subsequent sulfurization, the Mn 2p peaks of P,S–$MnMoO_4$ shift partially toward lower binding energies relative to P–$MnMoO_4$. This negative shift indicates an increase in electron density around Mn atoms, which can be attributed to the lower electronegativity of sulfur and its preferential occupation of oxygen-vacancy sites. Such sulfur-induced electronic enrichment stabilizes the local Mn coordination environment and reflects the transition from vacancy generation to vacancy stabilization. Overall, the stepwise evolution of Mn 2p binding energies-from pristine $MnMoO_4$ to P–$MnMoO_4$ and finally to P,S–$MnMoO_4$-provides

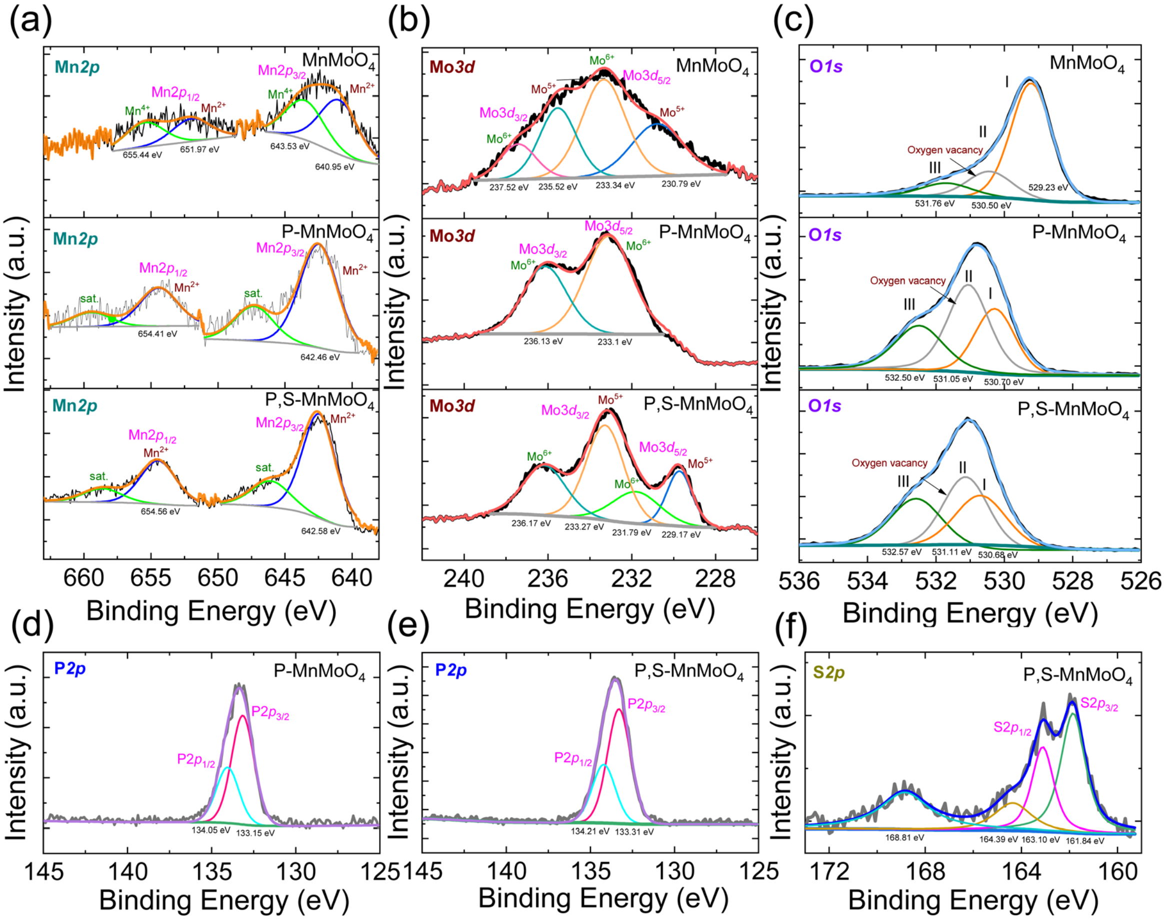

Fig. 4 High-resolution core-level XPS spectra of $MnMoO_4$-based electrocatalysts: (a) Mn 2p, (b) Mo 3d, (c) O 1s spectra of $MnMoO_4$, P–$MnMoO_4$ and P,S–$MnMoO_4$; (d and e) P 2p spectra of P–$MnMoO_4$ and P,S–$MnMoO_4$; and (f) S 2p spectrum of P, S–$MnMoO_4$.

direct spectroscopic evidence for phosphorus-driven oxygen-vacancy formation followed by sulfur-mediated defect stabilization, which plays a critical role in regulating the electronic structure and catalytic activity of $MnMoO_4$ toward acidic HER.

The Mo 3d spectra presented in Fig. 4(b) clearly shows two sets of doublets corresponding to Mo $3d_{5/2}$ and Mo $3d_{3/2}$. For $MnMoO_4$, the peaks positioned at 230.79 eV and 235.52 eV are attributed to Mo^{5+}, while the peaks at 233.34 eV and 237.52 eV are assigned to Mo^{6+}, corresponding to the Mo $3d_{5/2}$ and Mo $3d_{3/2}$, respectively. These results confirm the coexistence of Mo^{5+} and Mo^{6+} oxidation states within the $MnMoO_4$ structure. After phosphorization, two distinct peaks are observed at 233.1 eV and 236.13 eV, corresponding to the Mo^{6+} oxidation states of Mo $3d_{5/2}$ and Mo $3d_{3/2}$, respectively. In contrast to the $MnMoO_4$, only Mo^{6+} peaks are observed after phosphorization, indicating that Mo predominantly exists in the high-valent tetrahedral $MoO_4{}^{2-}$ state. This suggests that while Mo–O bonds are partially cleaved during the process, possibly it can form P–O bonds. Furthermore, following sulfurization, the partial substitution of oxygen with sulfur effectively promotes the reduction of Mo^{6+} to Mo^{5+} by increasing the local electron density around the Mo centers. As a result, the P,S–$MnMoO_4$ electrocatalyst exhibits both Mo^{5+} and Mo^{6+} oxidation states, with Mo^{5+} peaks observed at 229.17 eV (Mo $3d_{5/2}$) and 233.27 eV (Mo $3d_{3/2}$), and Mo^{6+} peaks at 231.79 eV (Mo $3d_{5/2}$) and 236.17 eV (Mo $3d_{3/2}$). The emergence of Mo^{5+} is attributed to the electron-donating nature of sulfur and the formation of defect-rich surfaces, both of which play a crucial role in enhancing the electronic conductivity of the catalyst.

The O 1s XPS spectra of $MnMoO_4$-based electrocatalysts are shown in Fig. 4(c). For pristine $MnMoO_4$, the O 1s spectrum can be deconvoluted into three components located at 529.23 eV, 530.50 eV, and 531.76 eV, which are assigned to lattice oxygen (O^{2-}), oxygen-vacancy-related oxygen species, and surface hydroxyl groups (–OH), respectively. The presence of the component at 530.50 eV indicates intrinsic oxygen vacancies within the $MnMoO_4$ lattice. After phosphorization, the corresponding O 1s peaks in P–$MnMoO_4$ shift to higher binding energies of 530.70 eV (lattice oxygen), 531.05 eV (oxygen-vacancy-related species), and 532.50 eV (surface hydroxyl groups). This positive shift reflects a decrease in local electron density around oxygen atoms induced by the incorporation of phosphorus species with higher electronegativity. Notably, the relative intensity of the oxygen-vacancy-related component increases markedly after phosphorization, indicating enhanced generation of oxygen vacancies due to the partial cleavage of Mn–O and Mo–O bonds and the formation of P–O coordination.

Following sulfurization, the O 1s peaks of P,S–$MnMoO_4$ are observed at 530.68 eV, 531.11 eV, and 532.57 eV, respectively. While the overall binding energies remain close to those of P–$MnMoO_4$, the relative intensity of the oxygen-vacancy-related peak decreases noticeably, suggesting partial passivation of oxygen vacancies by sulfur incorporation. This behavior indicates that sulfur preferentially occupies pre-formed oxygen-vacancy sites, stabilizing the defect structure and modulating the local electronic environment, which is consistent with the reduced ESR signal intensity observed after sulfurization. Direct evidence for heteroatom incorporation is provided by the P 2p and S 2p core-level spectra. As shown in Fig. 4(d), the P 2p spectrum of P–$MnMoO_4$ exhibits a well-resolved doublet at 133.15 eV (P $2p_{3/2}$) and 134.05 eV (P $2p_{1/2}$), which is characteristic of oxidized phosphorus species (phosphate-like P–O bonding) rather than metal phosphide. Importantly, after sulfurization (Fig. 4(e)), the corresponding P 2p peaks are retained and show only a slight positive shift to 133.31 eV and 134.21 eV, indicating that the phosphorus environment remains largely preserved while experiencing modest local electronic perturbation induced by subsequent sulfur incorporation. The persistence of the phosphate-like P–O signature after sulfurization supports the structural stability of incorporated phosphorus and suggests that P acts as a chemically robust component during the dual-step anion engineering process.[38] The S 2p spectrum of P,S–$MnMoO_4$ (Fig. 4(f)) further confirms sulfur incorporation. The doublet at 161.84 eV (S $2p_{3/2}$) and 163.10 eV (S $2p_{1/2}$) is attributed to metal–sulfur (S^{2-}) species, consistent with sulfur substitution/occupation at oxygen-deficient sites in the $MnMoO_4$ framework. In addition, higher-binding-energy components at 164.39 eV and 168.81 eV are assigned to oxidized sulfur species (SO_x/sulfate-like groups), likely resulted from partial surface oxidation upon exposure to air. Together, these features indicate successful sulfur incorporation with a minor fraction of oxidized sulfur at the surface.

Overall, the XPS results collectively support a stepwise and cooperative anion incorporation mechanism: phosphorization introduces stable P–O coordination while promoting oxygen-vacancy formation (as reflected by O 1s and ESR), and subsequent sulfurization introduces S^{2-} species that partially passivate vacancy-related defects and enrich the local electron density (as reflected by Mn/Mo core-level evolution). This regulated defect chemistry and electronic structure provides a favorable surface environment for charge transfer and hydrogen adsorption, thereby underpinning the enhanced acidic HER activity of P,S–$MnMoO_4$. Furthermore, the high-resolution XPS spectra of S–$MnMoO_4$ also provided (Fig. S5) clearly reveals the characteristic peaks corresponding to Mn, Mo, O, and S. The presence of distinct S 2p peaks, together with well-defined Mn 2p, Mo 3d, and O 1s peaks, indicates the successful sulfurization of $MnMoO_4$. Furthermore, the retention of the Mn and Mo core-level features suggests that the overall chemical framework of $MnMoO_4$ remains largely preserved after sulfurization. These results support the effective surface modification of $MnMoO_4$ through the sulfurization process. The quantitative analysis of all XPS spectra and the estimated oxygen vacancy concentrations, derived from deconvolution of the O 1s spectra, are summarized in Tables S1 and S2, respectively. The relative concentration of oxygen vacancies was calculated from the area ratio of the defect-related oxygen component to the total O 1s peak area, providing a comparative evaluation among the prepared electrocatalysts. In here, the relative defect-associated oxygen content increases significantly after phosphorization, while a slight decrease is observed following sulfur incorporation. This trend indicates that phosphorus modification correlates with increased defect-related oxygen species, whereas subsequent sulfurization alters the local surface environment. These observations are consistent with the improved HER performance of the dual-modified catalyst.

Overall, XPS and ESR analyses collectively indicate that the surface defect structure is modified through sequential P and S incorporation. It can be known that such electronic and defect-level adjustments are closely related to HER activity enhancement.

3.3. Electrochemical and kinetic analyses of $MnMoO_4$-based electrocatalysts for HER

The electrocatalytic HER performance of carbon cloth (CC), $MnMoO_4$, P–$MnMoO_4$, and P,S–$MnMoO_4$ was evaluated in N_2-saturated 0.5 M H_2SO_4 using iR-corrected polarization (*J*–*V*) curves, as shown in Fig. 5(a). The bare carbon cloth, serving as both the substrate and a control electrode, requires a high overpotential (η) of 738 mV_{RHE} to reach a current density of 10 mA cm^{-2}, indicating negligible intrinsic HER activity. Pristine $MnMoO_4$ exhibits a reduced overpotential of 536 mV_{RHE} at 10 mA cm^{-2}, reflecting its limited density of catalytically active sites and relatively poor electronic conductivity. Upon phosphorization, the overpotential is markedly decreased to 387 mV_{RHE} for P–$MnMoO_4$, suggesting that phosphorus incorporation effectively enhances HER activity. This improvement can be attributed to phosphorus-induced oxygen-vacancy formation and associated electronic-structure modulation, which collectively

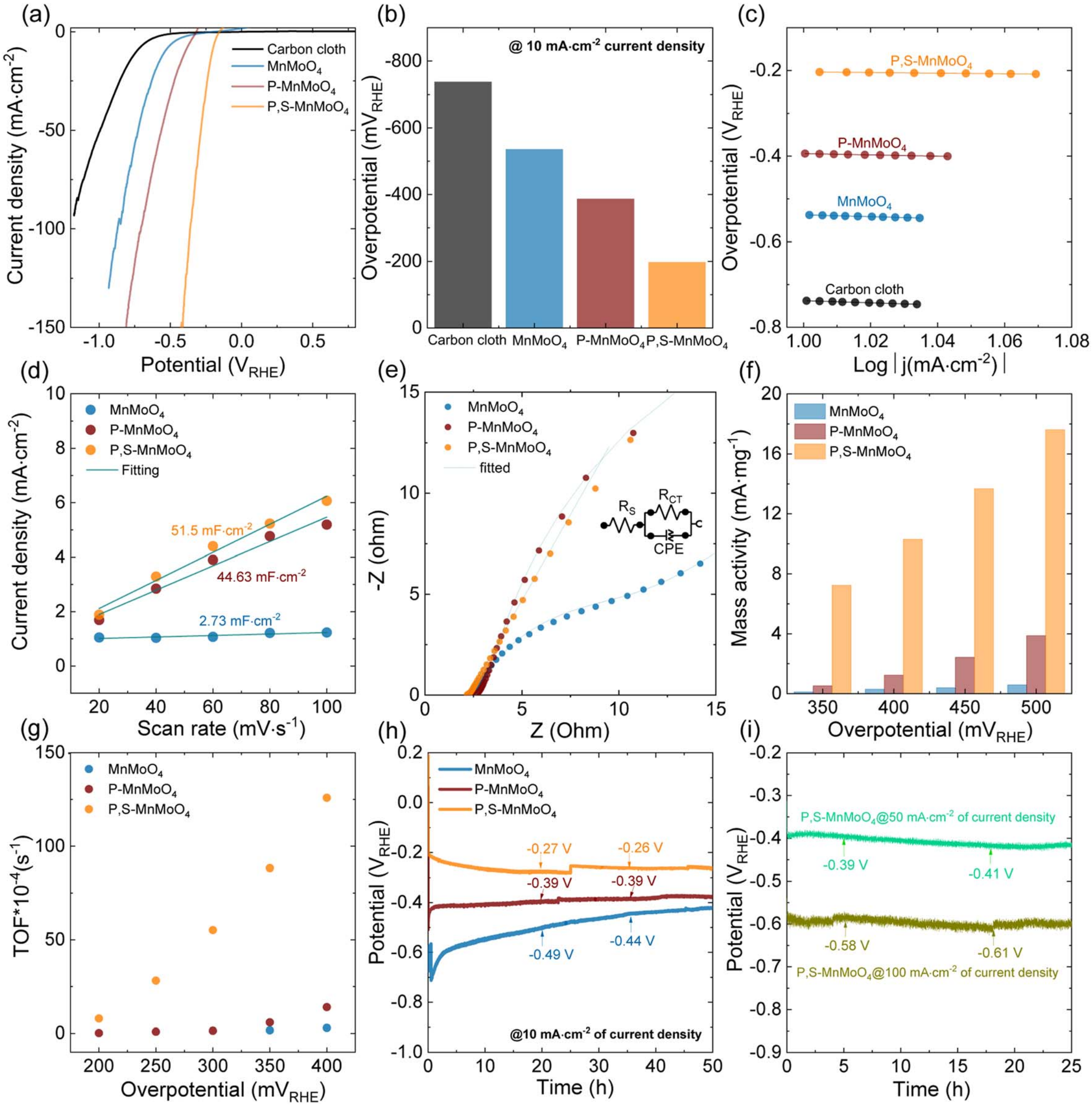

Fig. 5 Electrocatalytic HER performance of $MnMoO_4$-based electrocatalysts in acidic media: (a) *J*–*V* curves, (b) overpotentials required to achieve a current density of 10 mA cm^{-2} for each electrocatalyst, (c) Tafel plots derived from the corresponding *J*–*V* curves using linear fitting, (d) electrochemical active surface area (ECSA) by electrochemical double layer capacitance (C_{dl}), (e) Nyquist plots from EIS, with fitted results based on the equivalent circuit (inset), (f) comparison of mass activities, (g) comparison of the TOF values, (h) time-dependent chronopotentiometric stabilities of $MnMoO_4$, P–$MnMoO_4$, and P,S–$MnMoO_4$ electrocatalysts at the current densities of 10 mA cm^{-2}, and (i) time-dependent chronopotentiometric stabilities of P,S–$MnMoO_4$ electrocatalysts at the current densities of 50 mA cm^{-2} and 100 mA cm^{-2}.

facilitate charge transport and activate surface sites. Notably, the P,S–$MnMoO_4$ electrocatalyst delivers a substantially lower overpotential of only 198 mV_{RHE} at 10 mA cm^{-2}. The further enhancement compared to P–$MnMoO_4$ indicates that sulfur incorporation plays a synergistic role by preferentially occupying oxygen-vacancy sites, stabilizing defect structures, and optimizing hydrogen adsorption strength. These results demonstrate that the dual-step phosphorization–sulfurization strategy enables cooperative tuning of defect chemistry and electronic structure, thereby significantly boosting the HER performance of $MnMoO_4$ under acidic conditions. As summarized in Fig. 5(b), P,S–$MnMoO_4$ exhibits the lowest overpotential of 198 mV_{RHE} at 10 mA cm^{-2}, significantly outperforming pristine $MnMoO_4$ (536 mV) and P–$MnMoO_4$ (387 mV). For comparison, sulfurized $MnMoO_4$ without prior phosphorization (S–$MnMoO_4$, Fig. S6) exhibits an overpotential of 378 mV, while hydrogenated $MnMoO_4$ (H–$MnMoO_4$, Fig. S7) requires 437 mV to reach the same current density. Although sulfur modification improves activity relative to pristine $MnMoO_4$, neither sulfur treatment nor hydrogen-induced vacancy generation alone achieves the substantially lower overpotential observed for P,S–$MnMoO_4$. These comparative results indicate that sequential P and S incorporation provides the most favorable HER performance among the samples examined.

The reaction kinetics were further evaluated using Tafel analysis (Fig. 5(c)) and the Tafel plots were derived based on the Tafel equation, expressed as $\eta = b \log |J| + a$, where η denotes the overpotential (in mV), b is the Tafel slope (in mV dec^{-1}) reflecting the kinetics of the HER, J is the current density (in mA cm^{-2}), and is a reaction-dependent constant.[39] The Tafel slope serves as a key kinetic parameter that indicates the rate-determining step and the efficiency of electron transfer during electrocatalysis, the lower the slope, the faster the HER kinetics. P,S–$MnMoO_4$ exhibits the lowest Tafel slope of 75 mV dec^{-1}, markedly smaller than those of P–$MnMoO_4$ (149 mV dec^{-1}) and pristine $MnMoO_4$ (211 mV dec^{-1}), indicating substantially accelerated HER kinetics. For reference, the hydrogen evolution reaction generally proceeds through three elementary steps: the Volmer step (electrochemical proton adsorption), the Heyrovsky step (electrochemical desorption), and the Tafel step (chemical recombination), which are theoretically associated with Tafel slopes of approximately 120, 40, and 30 mV dec^{-1}, respectively.[40] The large Tafel slope of $MnMoO_4$ (211 mV dec^{-1}) suggests that HER is predominantly Volmer-limited, reflecting sluggish proton adsorption and limited availability of active sites. Upon phosphorization, the reduced slope of P–$MnMoO_4$ (149 mV dec^{-1}) indicates a partial enhancement in reaction kinetics, likely caused by phosphorus-induced oxygen vacancies that moderately improve charge transfer and surface reactivity. In contrast, the substantially lower Tafel slope of P,S–$MnMoO_4$ (75 mV dec^{-1}) implies a shift in the rate-determining step toward the Heyrovsky process, suggesting faster hydrogen desorption and more favorable interfacial charge-transfer dynamics. This kinetic transition can be attributed to sulfur-mediated electronic modulation, which optimizes hydrogen adsorption strength and stabilizes defect sites, thereby promoting more efficient HER kinetics.

To assess the density of accessible active sites, the electrochemically active surface area (ECSA) was estimated from the double-layer capacitance (C_{dl}) (Fig. 5(d) and S8). P,S–$MnMoO_4$ exhibits the highest C_{dl} of 51.5 mF cm^{-2}, exceeding those of P–$MnMoO_4$ (44.63 mF cm^{-2}) and $MnMoO_4$ (2.73 mF cm^{-2}). The corresponding ECSA values are calculated to be 1471 cm^2, 1275 cm^2, and 78 cm^2, respectively, demonstrating that dual P and S incorporation substantially increases the number of accessible catalytic sites.

Additionally, electrochemical impedance spectroscopy (EIS, Fig. 5(e)) further reveals enhanced interfacial charge transfer properties. The Nyquist plots, recorded at 0 V *vs.* RHE, were analyzed to quantify the interfacial charge-transfer characteristics of the electrocatalysts and the raw data were fitted using an equivalent circuit model to extract relevant electrochemical parameters, as shown in the inset of Fig. 5(e). This model consists of a series resistance (R_S), representing the inherent ohmic resistance of the electrolyte, wiring and contact interfaces; a charge-transfer resistance (R_{CT}), corresponding to the kinetic barrier for electron transfer between electrocatalyst surface and electrolyte; and a constant phase element (CPE), which replaces an ideal capacitor to model the non-ideal capacitive behavior commonly observed at rough or heterogeneous electrode interfaces. While all samples exhibit comparable solution resistance ($R_S \approx 2.2$–$2.6\ \Omega$), the charge-transfer resistance (R_{CT}) decreases dramatically from 76.55 Ω for $MnMoO_4$ to 3.40 Ω for P–$MnMoO_4$, and further to 0.52 Ω for P,S–$MnMoO_4$. This pronounced reduction indicates significantly improved interfacial charge-transfer kinetics in P,S–$MnMoO_4$, consistent with its enhanced HER performance.

As shown in Fig. 5(f and g) and Table 1, the mass activity and turnover frequency (TOF) of $MnMoO_4$, P–$MnMoO_4$, and P,S–$MnMoO_4$ were evaluated as function of overpotential to assess their intrinsic catalytic activity. Mass activity provides a normalized measure of catalytic performance per catalyst mass, while TOF reflects the reaction rate per active site. Among the three catalysts, P,S–$MnMoO_4$ exhibits consistently higher mass activity and TOF values than pristine $MnMoO_4$ and P–$MnMoO_4$ across the examined overpotential range. For example, at 400 mV, the mass activity of P,S–$MnMoO_4$ is approximately an order of magnitude higher than that of P–$MnMoO_4$ and significantly greater than that of pristine $MnMoO_4$. A similar trend is observed for TOF, where P,S–$MnMoO_4$ consistently delivers the highest turnover frequency of all evaluated potentials. Notably, the performance gap becomes more pronounced at higher overpotentials, indicating a sustained advantage in catalytic turnover under increasing driving force. In addition, the open-circuit potential (OCP) profiles of all catalysts were measured and are presented in Fig. S9. The OCP measurements provide complementary information on the interfacial equilibrium behavior of the electrodes under open-circuit conditions. Notably, P,S–$MnMoO_4$ shows a relatively steady OCP response compared with the other samples, which is consistent with its stable electrochemical performance under the tested conditions. These results confirm that dual P and S modification enhances the intrinsic catalytic activity beyond that achieved by single anion modification.

Table 1 Summary of mass activity and TOF values obtained from Fig. 5(f and g)

	Mass activity (mA mg^{-1})				TOF × 10^{-4} (s^{-1})				
	Overpotential (mV_{RHE})				Overpotential (mV_{RHE})				
Catalyst	350	400	450	500	200	250	300	350	400
$MnMoO_4$	0.11	0.29	0.39	0.58	—	—	—	1.66	2.95
P–$MnMoO_4$	0.52	1.23	2.42	3.86	0.21	0.91	1.39	5.86	14
P,S–$MnMoO_4$	7.24	10.29	13.67	17.62	7.90	28.17	55.21	88.33	125.9

The long-term durability of $MnMoO_4$, P–$MnMoO_4$, and P,S–$MnMoO_4$ was assessed by chronopotentiometry at a constant current density of 10 mA cm^{-2} (Fig. 5(h)). The P,S–$MnMoO_4$ catalyst maintains a nearly constant potential of approximately 0.26 to 0.27 V *vs.* RHE over 50 h, with no noticeable fluctuations during continuous operation under acidic HER conditions. Under the same conditions, P–$MnMoO_4$ exhibited stable behavior at a higher potential of around 0.39 V *vs.* RHE, while pristine $MnMoO_4$ required an even higher potential (0.44 V to 0.49 V *vs.* RHE) to sustain the same current density. P,S–$MnMoO_4$ operates at a lower overpotential while maintaining stable performance over extended electrolysis compared with the single-modified and unmodified catalysts. The potential difference among the catalysts reflects the improved activity of P,S–$MnMoO_4$ under identical stability testing conditions.

Furthermore, the long-term durability of P,S–$MnMoO_4$ was evaluated at elevated current densities of 50 and 100 mA cm^{-2} for 25 h (Fig. 5(i)). The electrode maintained nearly constant potentials of 0.39 V and 0.58 V *vs.* RHE at 50 and 100 mA cm^{-2}, respectively, with only a slight potential shift (approximately 20–30 mV) over the testing period. No abrupt fluctuations or significant degradation were observed during continuous operation. Such stable chronopotentiometric behavior at relatively high current densities indicates sustained catalytic activity under prolonged electrolysis conditions. For comparison, pristine $MnMoO_4$ and P–$MnMoO_4$ exhibited higher operating potentials and more noticeable fluctuations at 50 mA cm^{-2} under identical testing conditions (Fig. S10), suggesting comparatively lower stability. These results demonstrate that P,S–$MnMoO_4$ maintains stable electrochemical performance at both moderate and high current densities in acidic media over extended operation.

To assess the possible morphological changes after prolonged HER operation, the post-electrolysis FE-SEM analyses were conducted following 50 h of continuous testing at 10 mA cm^{-2} (Fig. S11). The $MnMoO_4$ and P–$MnMoO_4$ largely retained their plate-like morphology, while P,S–$MnMoO_4$ exhibits a slightly roughened surface texture after prolonged operation. Nevertheless, no apparent structural collapse or fragmentation was observed. For the P,S–$MnMoO_4$ tested at higher current densities of 50 and 100 mA cm^{-2} for 25 h (Fig. S12), the overall morphology remains comparable to that of the pre-tested sample, without noticeable microstructural degradation. The relatively smoother appearance compared to the 50 h sample may be attributed to the shorter testing duration. Overall, the FE-SEM observations indicate that no severe morphological degradation occurs under the acidic HER examined conditions.

Furthermore, post-stability core-level XPS analysis was conducted to investigate the surface chemical states after prolonged HER operation at 10 mA cm^{-2} for 50 h (Fig. S13). Compared with the pristine samples prior to stability testing (Fig. 4), slight shifts were observed in the Mn 2p spectra of $MnMoO_4$, P–$MnMoO_4$, and P,S–$MnMoO_4$ after long-term electrolysis (Fig. S13(a)), suggesting minor alterations in the local electronic environment of Mn during extended operation.[10] Notably, the Mn^{4+} peak, which likely originated from synthesis or air exposure, disappeared in $MnMoO_4$ after stability testing. In contrast, the P- and P,S-modified samples largely retained their original valence states, demonstrating enhanced structural robustness upon heteroatom incorporation. Furthermore, only negligible shifts were observed in the Mo 3d and O 1s spectra (Fig. S13(b and c)) for all three electrocatalysts, providing strong evidence for their maintained structural integrity. Specifically, for P–$MnMoO_4$, the Mo 3d peaks exhibit a shift to lower binding energies at 231.64 eV and 234.79 eV and slight change in relative peak intensity observed after stability test indicating a slight reduction in Mo's oxidation state or minor surface reconstruction or electronic redistribution during long term electrochemical operation. Additionally, the P 2p and S 2p spectra (Fig. S13(d–f)) verify the persistent presence of P in P–$MnMoO_4$ and P,S–$MnMoO_4$, as well as S in P,S–$MnMoO_4$, following long-term electrolysis. Overall, these results indicate that both the structural framework and heteroatom incorporation remain stable under HER conditions, thereby supporting the excellent durability of the catalysts. Quantitative analysis of all XPS spectra is summarized in Table S3. Overall, the electrochemical results demonstrate that vacancy-mediated dual anion engineering simultaneously lowers the thermodynamic overpotential, accelerates HER kinetics, increases the active surface area, and enhances long-term stability, establishing P,S–$MnMoO_4$ as an efficient and robust acidic HER electrocatalyst.

3.4. Unveiling the origin of superior HER activity in P,S–$MnMoO_4$ *via* dual-anion and defect engineering: a theoretical study

To provide an atomic-level understanding of the superior HER performance and structural stability achieved by the dual anion incorporation of P and S into $MnMoO_4$, comprehensive density functional theory (DFT) calculations were performed. The experimental evidence, specifically the ESR and XPS results indicating the presence of oxygen vacancies (V_O) and the successful incorporation of phosphorus and sulfur, was used to construct five representative surface models based on the (001) facet of β-$MnMoO_4$. The models constructed were as follows Fig. 6(a) and S14: (i) pristine $MnMoO_4$, (ii) oxygen-deficient $MnMoO_4$ (V_O–$MnMoO_4$), (iii) P–$MnMoO_4$ with oxygen vacancies (P + V_O–$MnMoO_4$), (iv) P,S–$MnMoO_4$ synthesized *via* dual-step phosphorization-sulfurization, and (v) sulfurized $MnMoO_4$ (S–$MnMoO_4$).

A systematic evaluation of the thermodynamic preference for incorporation sitting was conducted to validate the synthesized structures (Fig. S15(a)). To identify the most favorable configuration, the incorporation formation energies for phosphorus at four distinct interstitial sites (denoted as Sites I–IV) within the $MnMoO_4$ lattice were calculated. As shown in Fig. S15(b), the calculated formation energies are −1.38 eV for Site I, 0.27 eV for Site II, −2.29 eV for Site III, and 0.12 eV for Site IV. Notably, Site III exhibits the lowest formation energy, indicating that phosphorus incorporation at this interstitial position is the most exothermic and thermodynamically stable process. Consequently, Site III was adopted as the representative phosphorus incorporated sites for all subsequent P-incorporated models. A critical finding from our calculations is the cooperative relationship between phosphorus incorporation, oxygen-vacancy formation, and sulfur substitution. The V_O formation energy on pristine $MnMoO_4$ is 3.03 eV, whereas in the P–$MnMoO_4$ lattice it slightly decreases to 2.93 eV. When referenced to pristine $MnMoO_4$, the configuration containing both interstitial P and an oxygen vacancy lies only 0.64 eV higher in energy, demonstrating that vacancy formation is thermodynamically compatible with phosphorus incorporation as shown in Fig. 6(b). Upon sulfurization, filling a pre-formed V_O on pristine $MnMoO_4$ with sulfur is exothermic with a reaction energy of −0.84 eV, yielding a sulfur-substitute structure that is 2.19 eV above pristine $MnMoO_4$. In contrast, sulfur incorporation into a V_O in the P–$MnMoO_4$ lattice is even more favorable, with a reaction energy of −1.13 eV and a final P, S co-incorporated structure that is stabilized to −0.49 eV relative to pristine $MnMoO_4$ as shown in Fig. 6(b). This enhanced exothermicity signifies a strong thermodynamic driving force for sulfur to occupy vacancies in the P–$MnMoO_4$ lattice. Consequently, these thermodynamic results support a vacancy-mediated co-incorporation mechanism (Fig. 6(b)), confirming that the synergistic interaction between P and S incorporation stabilizes the $MnMoO_4$ framework and underpins the structural robustness of the P, S co-incorporated phase.

Conventional DFT studies generally evaluate the Gibbs free energy of hydrogen adsorption (ΔG_{H^*}) on pristine surfaces. However, these simplified models frequently lack the capacity

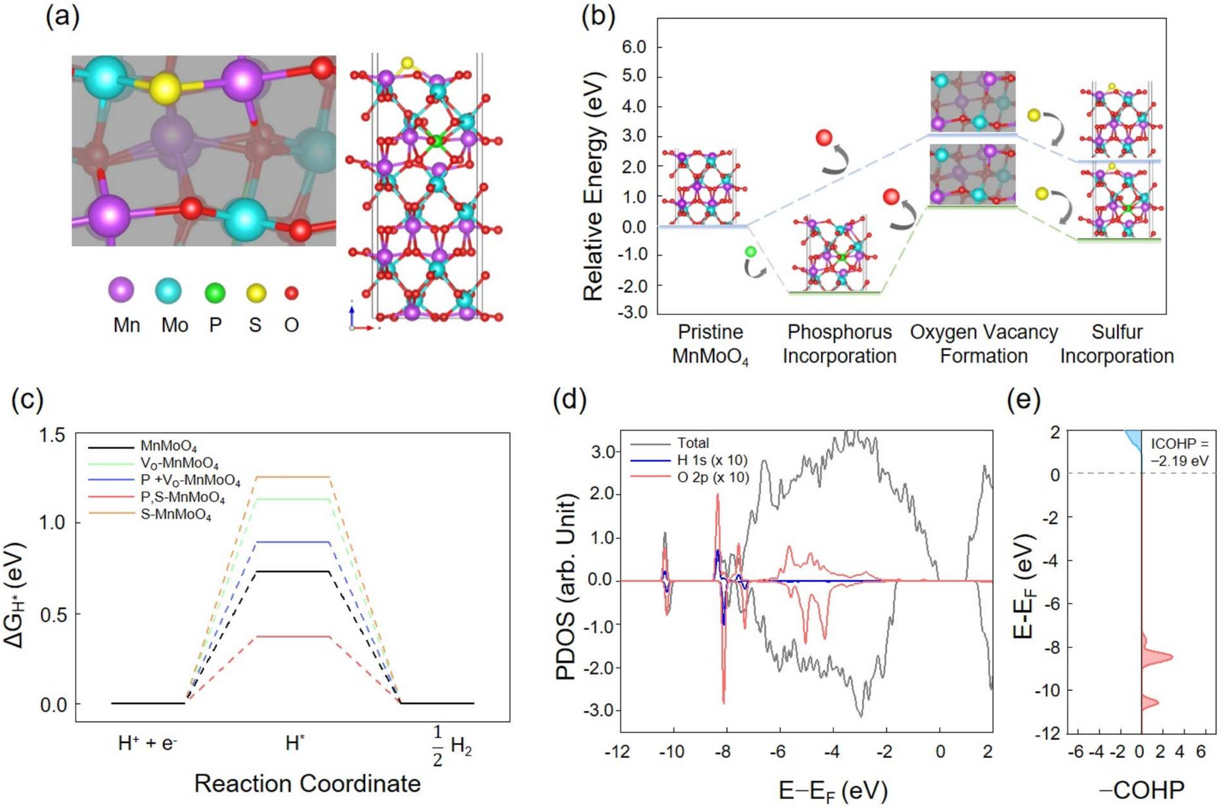

Fig. 6 (a) Representative surface model of P,S–$MnMoO_4$, (b) relative energies for the vacancy-mediated co-incorporation mechanism in the prepared electrocatalysts, (c) reaction coordinate diagram for $MnMoO_4$, Vo–$MnMoO_4$, P + Vo–$MnMoO_4$, P,S–$MnMoO_4$ and S–$MnMoO_4$, (d) projected density of states (PDOS) for the adsorbed H and (e) crystal orbital Hamilton population (COHP) and integrated COHP (ICOHP) values for P,S–$MnMoO_4$.

to accurately represent the realistic *operando* surface state of metal oxides in acidic media. In order to rigorously satisfy the fundamental definition of a catalyst which requires the return to an identical initial state after a reaction cycle, the starting surface must represent a thermodynamically stable phase under reaction conditions. As demonstrated in Fig. S16, our systematic adsorption calculations reveal that the initial four hydrogen atoms (1H* to 4H*) manifest strongly negative adsorption energies ($\Delta G < 0$). A thorough structural analysis reveals that these protons exhibit a strong preference for binding to surface oxygen atoms, resulting in stable surface hydroxylation rather than participating in the catalytic turnover. Therefore, we propose that these strongly bound hydrogen species function as static surface modifiers, thereby reconfiguring the electronic landscape, rather than operating as active intermediates. In light of the aforementioned findings, it is imperative to delineate the pre-hydrogenated surface (covered with 4H*) (Fig. S17) as the thermodynamically salient active state. The adsorption of the fifth hydrogen atom (5H*) is instrumental in the initiation of the catalytic turnover involving metal active sites (Fig. S18).

In adopting this hydrogenated surface model, the ΔG_{H^*} for the rate-determining fifth H^* adsorption step was calculated. As demonstrated in the reaction coordinate diagram (Fig. 6(c)), the performance of the catalyst is found to be highly sensitive to the local coordination environment. The pristine $MnMoO_4$ and singly with only vacancy or single doped models (V_O–$MnMoO_4$, P + V_O–$MnMoO_4$, S–$MnMoO_4$) exhibited unfavorable binding energetics for the fifth hydrogen, showing too weak binding, which corresponds to a high theoretical overpotential. Notably, the P,S–$MnMoO_4$ catalyst exhibited a ΔG_{H^*} value of 0.37 eV, which is the closest to the optimal value (ΔG_{H^*} approximately 0 eV) among all the investigated systems. In order to elucidate the electronic origin of this optimized binding, an electronic structure analysis was conducted on P,S–$MnMoO_4$ and pristine $MnMoO_4$, the latter of which exhibited the next-closest value (0.73 eV) to the optimal value. The projected density of states (PDOS) for the 5th adsorbed H and the corresponding active sites were analyzed, as illustrated in Fig. 6(d) and S11(a). For clarity, the PDOS intensity for the H 1s-orbital and active site orbitals was magnified 10 times. Although orbital overlaps between the H 1 s orbital and the active site states are observed in both pristine $MnMoO_4$ (Fig. S19(a)) and P,S–$MnMoO_4$ (Fig. 6(d)), distinguishing the precise strength of this hybridization requires a more quantitative analysis using crystal orbital Hamilton population (COHP).[41] The COHP curves and integrated COHP (ICOHP) values, calculated over the energy range of −12 to 0 eV (Fig. 6(e) and S19(b)), reveal that the P,S–$MnMoO_4$ system exhibits significantly stronger orbital hybridization between the active site and the H* intermediate compared to the pristine $MnMoO_4$ (Fig. S11(b)). This enhanced hybridization effectively stabilizes the catalyst surface–hydrogen bond, thereby increasing the adsorption energy. As a result, P,S–$MnMoO_4$ achieves the strongest binding affinity ($\Delta G_{H^*} = 0.37$ eV) among the models, effectively minimizing the thermodynamic barrier for the Volmer step where the actual catalytic turnover initiates.

Consequently, our theoretical results provide conclusive evidence that the superior HER activity of P,S–$MnMoO_4$ arises from a dual-step synergy: (1) P insertion facilitates the formation of stable S-occupied oxygen vacancy sites (V_O). (2) the coexistence of P and S electronically enhances the orbital hybridization on the working-state hydrogenated surface, thereby optimizing the adsorption kinetics.

4. Conclusion

In summary, we have developed a rational dual-step phosphorization-sulfurization strategy to transform pristine $MnMoO_4$ into a heteroatom-enriched P,S–$MnMoO_4$ electrocatalyst with outstanding hydrogen evolution reaction (HER) performance in acidic media. $MnMoO_4$ was first synthesized *via* a hydrothermal method, followed by sequential phosphorization and sulfurization to introduce phosphorus and sulfur into the oxide framework. This dual-anion incorporation synergistically tailors the electronic structure, enhances electrical conductivity, and substantially increases the electrochemically active surface area, leading to accelerated charge-transfer kinetics and a higher density of accessible active sites. As a result, the optimized P,S–$MnMoO_4$ catalyst delivers a low overpotential of 198 mV_{RHE} at 10 mA cm^{-2}, significantly outperforming pristine $MnMoO_4$ (536 mV_{RHE}), while maintaining excellent operational stability over 50 h. Density functional theory (DFT) calculations further elucidate the origin of the enhanced HER activity. Phosphorus incorporation thermodynamically facilitates oxygen-vacancy formation and stabilizes subsequent sulfur occupation, giving rise to robust P,S-coordinated active sites that are stable under acidic conditions. Importantly, when a realistic hydrogenated surface is considered as the *operando* catalytic state, the cooperative presence of P and S markedly enhances orbital hybridization between the active sites and adsorbed H*, resulting in an optimized hydrogen adsorption free energy (ΔG_{H^*}). This near-ideal ΔG_{H^*} lowers the thermodynamic barrier for the Volmer step, promotes efficient electron transfer, and enables rapid H* adsorption–desorption kinetics. Overall, this work demonstrates that vacancy-mediated dual-anion engineering provides an effective route to simultaneously optimize activity and durability in metal–oxide electrocatalysts. The insights presented herein offer clear theoretical guidance and a scalable design paradigm for developing high-performance, earth-abundant electrocatalysts toward sustainable hydrogen production.

Author contributions

Jyoti Ganapati Badiger: experiments, synthesis, characterization, writing. Chae-Eun Lim: DFT calculations, DFT writing, formal analysis. Fawad Tariq: experiment, formal analysis. Maheswari Arunachalam: formal analysis and editing. Suzan Abdelfattah Sayed: formal analysis. Alaa M. Ibrahim: formal analysis. Sang Wan Ryu: writing – review and editing. Byung-Hyun Kim: writing – review and editing, Soon Hyung Kang: project administration, writing – review and editing.

Conflicts of interest

The authors declare that they have no known competing financial interests or personal relationships that could have appeared to influence the work reported in this article.

Data availability

The data supporting this study are available within the article and its supplementary information (SI). Additional data related to this work are available from the corresponding author upon reasonable request.

Supplementary information is available. See DOI: https://doi.org/10.1039/d6ta01695b.

Acknowledgements

This research was supported by grants (2018R1A6A1A03024334, RS-2025-00523371, 2022M3C1A3092056) of the Korea Science Research Program through the National Research Foundation of Korea and a Grant (RS-2025-02413029) funded by Korea Basic Science Institute (National research Facilities and Equipment Center) of the Ministry of Education. The authors express their gratitude to the Center for Research Facilities at Chonnam National University for their assistance in the analysis of the $MnMoO_4$ films using FE-SEM, XPS and XRD. The authors also acknowledge the Korea Institute of Science and Technology Information (KISTI) for providing the computational resources used in this research.

References

1 N. Sazali, *Int. J. Hydrogen Energy*, 2020, **45**, 18753–18771.
2 J. G. Badiger, S. S. Subramanian, M. Arunachalam, R. S. Kanase, S. A. Sayed, G. H. Gu and S. H. Kang, *J. Power Sources*, 2025, **652**, 237580.
3 R. S. Kanase, M. Arunachalam, J. Badiger, P. K. Das and S. H. Kang, *ACS Appl. Energy Mater.*, 2022, **5**, 13913–13927.
4 M. Arunachalam, R. Subhash Kanase, J. Ganapati Badiger, S. Abdelfattah Sayed, K.-S. Ahn, J.-S. Ha, S.-W. Ryu and S. Hyung Kang, *Chem. Eng. J.*, 2023, **474**, 145262.
5 H. Huang, M. Yan, C. Yang, H. He, Q. Jiang, L. Yang, Z. Lu, Z. Sun, X. Xu, Y. Bando and Y. Yamauchi, *Adv. Mater.*, 2019, **31**, 1903415.
6 H. Jiang, K. Zhang, W. Li, Z. Cui, S.-A. He, S. Zhao, J. Li, G. He, P. R. Shearing and D. J. L. Brett, *J. Power Sources*, 2020, **472**, 228497.
7 Z. Xiao, J. Wang, C. Liu, B. Wang, Q. Zhang, Z. Xu, M. T. Sarwar, A. Tang and H. Yang, *Appl. Surf. Sci.*, 2022, **602**, 154314.
8 Z. Gao, T. Shen, Z. Zeng, S. Chang, Z. Guo, X. Xu, Y. Li, D. Wu and R. Jia, *J. Colloid Interface Sci.*, 2025, **677**, 569–576.
9 Q. Wu, L. Chen, D.-H. Kuo, P. Li, A. B. Abdeta, O. A. Zelekew, J. Lin and X. Chen, *ACS Appl. Mater. Interfaces*, 2023, **15**, 22142–22156.
10 J. G. Badiger, M. Arunachalam, R. S. Kanase, S. A. Sayed, K.-S. Ahn, J.-S. Ha and S. H. Kang, *Int. J. Hydrogen Energy*, 2024, **51**, 156–168.
11 X. Yan, L. Tian, J. Murowchick and X. Chen, *J. Mater. Chem. A*, 2016, **4**, 3683–3688.
12 C. Sun, H. Yin, X. Xing, Y. Lv, W. Xiong and H. Li, *Ind. Eng. Chem. Res.*, 2025, **64**, 8759–8767.
13 S. A. Patil, D. V. Patil, A. I. Inamdar, S. Hussain, J. Jung, H. Im, N. K. Shrestha, S. Cho and J.-W. Jang, *J. Power Sources*, 2025, **653**, 237661.
14 H. Wang, Y. Song, J. Zhou, X. Xu, W. Hong, J. Yan, R. Xue, H. Zhao, Y. Liu and J. Gao, *Electrochim. Acta*, 2016, **212**, 775–783.
15 M. S. Tamboli, S. A. Patil, A. M. Tamboli, S. S. Patil, N. T. N. Truong, K. Lee, C. S. Praveen, N. K. Shrestha, C. Park and B. B. Kale, *Dalton Trans.*, 2022, **51**, 6027–6035.
16 G. Kresse and J. Furthmüller, *Comput. Mater. Sci.*, 1996, **6**, 15–50.
17 G. Kresse and J. Hafner, *Phys. Rev. B:Condens. Matter Mater. Phys.*, 1993, **47**, 558–561.
18 G. Kresse and J. Hafner, *Phys. Rev. B:Condens. Matter Mater. Phys.*, 1994, **49**, 14251–14269.
19 G. Kresse and D. Joubert, *Phys. Rev. B:Condens. Matter Mater. Phys.*, 1999, **59**, 1758–1775.
20 J. P. Perdew, K. Burke and M. Ernzerhof, *Phys. Rev. Lett.*, 1996, **77**, 3865–3868.
21 S. Grimme, J. Antony, S. Ehrlich and H. Krieg, *J. Chem. Phys.*, 2010, **132**, 154104.
22 H. J. Monkhorst and J. D. Pack, *Phys. Rev. B*, 1976, **13**, 5188–5192.
23 S. Lei, K. Tang, Q. Liu, Z. Fang, Q. Yang and H. Zheng, *J. Mater. Sci.*, 2006, **41**, 4737–4743.
24 C. Zhang, D. Wu, L. Shi, Y. Zhu, D. Xiong, S. Xu, R. Huang, R. Qi, W. Zhang, L. Wang and P. K. Chu, *R. Soc. Open Sci.*, 2017, **4**(12), 171229.
25 S. Aswathappa, L. Dai, S. Sahaya Jude Dhas, S. A. Martin Britto Dhas, P. Sengodan and R. S. Kumar, *J. Mater. Res. Technol.*, 2024, **30**, 1696–1705.
26 S. L. Dudarev, G. A. Botton, S. Y. Savrasov, C. J. Humphreys and A. P. Sutton, *Phys. Rev. B:Condens. Matter Mater. Phys.*, 1998, **57**, 1505–1509.
27 Y.-C. Wang, Z.-H. Chen and H. Jiang, *J. Chem. Phys.*, 2016, **144**, 144106.
28 C. Franchini, R. Podloucky, J. Paier, M. Marsman and G. Kresse, *Phys. Rev. B:Condens. Matter Mater. Phys.*, 2007, **75**, 195128.
29 R. Coquet and D. J. Willock, *Phys. Chem. Chem. Phys.*, 2005, **7**, 3819–3828.
30 T. Zeng, X.-D. Wen, G.-S. Wu, Y.-W. Li and H. Jiao, *J. Phys. Chem. B*, 2005, **109**, 2846–2854.
31 B. E. Conway and M. Salomon, *Electrochim. Acta*, 1964, **9**, 1599–1615.
32 J. K. Norskov, T. Bligaard, A. Logadottir, J. Kitchin, J. G. Chen, S. Pandelov and J. Norskov, *J. Electrochem. Soc.*, 2005, **152**, J23–J26.

33 J. K. Nørskov, J. Rossmeisl, A. Logadottir, L. Lindqvist, J. R. Kitchin, T. Bligaard and H. Jónsson, *J. Phys. Chem. B*, 2004, **108**, 17886–17892.

34 Y. Liu, Y. Li, Z. Liu, T. Feng, H. Lin, G. Li and K. Wang, *Molecules*, 2024, **29**, 1988.

35 H. Yin, X. Xing, W. Zhang, J. Li, W. Xiong and H. Li, *Dalton Trans.*, 2023, **52**, 16670–16679.

36 J. Huang, J. Zeng, K. Zhu, R. Zhang and J. Liu, *Nano-Micro Lett.*, 2020, **12**, 110.

37 Y. Dou, L. Zhao, J. Wang, S. Li, Y. Zhang, R. Li, M. Gao, C. Zhang and Z. Guo, *eScience*, 2025, 100434, DOI: 10.1016/j.esci.2025.100434.

38 L. Wang, Y. Zhao, H. Chen, Y. Yang, D. Wang, H. Shang and B. Zhang, *J. Colloid Interface Sci.*, 2025, **677**, 167–177.

39 L. Zhang, M. Li, A. Zou, S. H. Yu, T. Xiong, L. Wang, J. He, Q. Fu, K. Sun, D. H. C. Chua and J. Xue, *ACS Appl. Energy Mater.*, 2019, **2**, 493–502.

40 G. Zhang, A. Wang, L. Niu, W. Gao, W. Hu, Z. Liu, R. Wang and J. Chen, *Adv. Energy Mater.*, 2022, **12**, 2103511.

41 V. L. Deringer, A. L. Tchougréeff and R. Dronskowski, *J. Phys. Chem. A*, 2011, **115**, 5461–5466.